Metasurface Antennas Design: Full-Wave Feeder Modeling and Far-Field Optimization

Jean Cavillot, *Member, IEEE*, Modeste Bodehou, *Member, IEEE*, and Christophe Craeye, *Senior Member, IEEE*

***Abstract*— This article addresses the optimization of the radiation pattern of surface-wave (SW)-based metasurface (MTS) antennas. Those antennas are considered a promising alternative to parabolic reflectors and phased arrays due to their extremely low profile and their ability to provide high gain, shaped beams and multibeams. However, pattern synthesis with MTS antennas is very challenging because of the single active control point and the need to control surface and leaky waves through the MTS. An accurate optimization of the radiation pattern, along with the sidelobe level requires full-wave modeling of the feeding structure, including its coupling with the MTS. MTS synthesis methods existing in the literature usually approximate the feeder model, and neglect its coupling with the MTS. Such approximation may lead to more than 1 dB error in the predicted antenna directivity. This article presents a technique for optimization of the far-field pattern, built on a Method of Moments (MoM) analysis tool in which the MTS coupling with the feeder, a coax probe, is fully considered. The MTS is modeled as an arbitrarily shaped, spatially modulated electric sheet impedance in a layered medium. At each optimization iteration, the complexity of the underlying analysis is $\mathcal{O}(N \log N)$ owing to the use of a fast Fourier transforms (FFT)-based acceleration. The effectiveness of the method is demonstrated through the optimization of MTSs radiating a pencil beam and a conical beam with orbital angular momentum (OAM).**

***Index Terms*— Broken rooftop, fast Fourier transforms (FFT), impedance boundary condition (IBC), magnetic frill, metasurfaces (MTSs), method of moments (MoM).**

I. Introduction

METASURFACES (MTSs) are revolutionizing the field of waves engineering, not only in electromagnetics [1], but also in acoustics [2]. The basic idea behind this new technology lies in synthesizing thin artificial surfaces (i.e., with sub-wavelength texture and thickness) capable of presenting, at the wavelength of operation, properties that go beyond those usually found in nature [3]. Among various applications of MTSs in electromagnetics, MTS antennas have experienced rapid development over the past decade [4], [5], [6], [7], [8], [9], [10], [11], [12], [13]. A MTS can be used to redirect the wave coming from an initial antenna, [4], [5] or to act as a lens [6], [7], [8]. Furthermore, MTSs can also be designed to manipulate the dispersion characteristics of surface waves (SWs) [9], [10], [11], [12], [13]. In the latter case, the feeder is an SW launcher integrated into the MTS plane. That configuration makes the antenna profile particularly low as compared to reflectarrays or transmitarrays. SW-based MTS antennas are typically fed by a TM polarized source, usually, a coax probe [10], [11]. The MTS implements a spatially modulated surface impedance, which progressively transforms the SW into leaky waves. Pattern synthesis with MTSs is more challenging than with dense antenna arrays, because of the single active control point and given the need to manipulate the surface and leaky waves through the surface impedance modulation. In particular MTS antennas being based on leaky waves, a difficult tradeoff needs to be established between the directivity, which requires homogeneous aperture illumination and limitation of SW diffraction at the rim of the antenna.

Recently, fast analysis tools have been developed to rapidly predict the far-field radiation from MTS antennas [14], [15], [16]. Those tools usually assume the MTS to be of canonical shape (circular, elliptical, etc.), so as to properly model the current distribution on the surface with relatively few basis functions. More recently, an efficient method capable of analyzing arbitrarily shaped MTSs has been proposed [17]. In that novel approach, the current distribution is expanded into rooftop basis functions disposed on a regular grid. The regularity of the mesh is exploited to drastically reduce the computation complexity (almost linear in practice) and the required memory. As a consequence, very large and arbitrarily shaped MTS antennas meshed with more than 1 million basis functions can be analyzed in a few minutes on a conventional computer [17]. However, in all the previous works, the feeder is not fully modeled. A point source modeling of the feeder is usually assumed. Although this modeling allows for rapid estimation of the radiation pattern, it fails at predicting the antenna input impedance and may introduce inaccuracies (about 2 dB error) on the predicted antenna gain and sidelobe level.

This article extends the method developed in [17], by providing a full model of the feeder and of its coupling with the MTS, while enabling rapid optimization of the MTS. The proposed novel tool is capable of rapidly predicting the antenna far-field, as well as its input impedance. It includes a fine analysis of fields near basis functions that connect the

Manuscript received 29 December 2021; revised 13 September 2022; accepted 19 September 2022. Date of publication 10 October 2022; date of current version 19 January 2023. This work was supported in part by the Fonds pour la Formation à la Recherche dans l'Industrie et dans l'Agriculture (FRIA) Grant and in part by the Chargé de Recherches Program from the Belgium Fonds National de la Recherche Scientifique (FNRS). *(Corresponding author: Jean Cavillot.)*

The authors are with ICTEAM, École Polytechnique de Louvain, Université Catholique de Louvain, 1348 Ottignies-Louvain-la-Neuve, Belgium (e-mail: jean.cavillot@uclouvain.be).

Color versions of one or more figures in this article are available at https://doi.org/10.1109/TAP.2022.3211735.

Digital Object Identifier 10.1109/TAP.2022.3211735

feeding pin with its extension printed on the dielectric slab. Relying on this tool, on the analytical MTS solutions proposed in [10], and on the integral equation-based numerical design technique proposed in [12], an optimization method is developed to satisfy far-field specifications (directivity, sidelobe level, etc.) for pencil and shaped beams. This optimization requires the update of the MTS only and, as will be shown, can be carried out relatively fast (N log N complexity at each optimization iteration, N being the number of basis functions), while fully models the feeder coupling with the MTS. Besides, in the example shown here, the input impedance of the antenna is very close to the one obtained with the feeder alone (i.e., the coupling from the MTS to the feeder can be neglected). The sequel of this article is structured as follows. Section II presents the feeder modeling and shows validation of the feeder model with simulations obtained using the CST commercial software [18] on a rectangular patch antenna. Section III details and validates the method of moments (MoM) formulation. The computation time of the method as well as the coupling between the feeder and the MTS are also analyzed. Section IV presents an optimization algorithm for the MTS efficiency based on a nonuniform modulation index. The optimization scheme is also proposed with another model of the nonuniform modulation in order to reduce the sidelobe level in Section V. Finally, Section VI draws the conclusions.

II. Coax-Feed Modeling

A. Description of the Feeder Model

This section briefly explains the adopted MoM modeling of the coax feeder and presents numerical validations of the feeder model with the frequency domain solver of the CST commercial software. The proposed feeder model is thereafter used in Section III to analyze coax-fed MTS antennas. In the following, it is assumed that the reader is familiar with the MoM for solving Maxwell equations in integral equation form in layered media [19], [20], [21].

Let us consider a coax-fed planar antenna as schematically represented in Fig. 1. The antenna metallization lies on an infinite grounded dielectric slab of thickness d and relative permittivity ϵ_d. The metallic parts are modeled as 0-thickness perfect electric conductor. The signal is sent through a coaxial cable with an inner radius of r_a and outer radius r_b. It is assumed that the coax line is designed so as to support the propagation of the fundamental mode only in the frequency band of interest. A planar patch, called "feeder extension" in Fig. 1, is connected to the inner conductor of the coax. This patch can have an arbitrary shape and its dimensions can be adjusted for impedance matching purposes.

Extensive efforts have been devoted to the analysis and modeling of vertical conductors in layered media [22], [23], [24], [25]. Analytical methods based on cavity models [26], [27] and integral-equations methods assuming a uniform probe current distribution [28] were developed. While these methods yield satisfactory results for electrically thin substrates, they are not able to accurately predict the input impedance of coax-fed antennas printed on electrically thick substrates, which is the case for pin-fed MTSs. In order to fix this issue, models using basis functions on the vertical conductors have emerged [29]. The use of basis functions allows accurate description of the

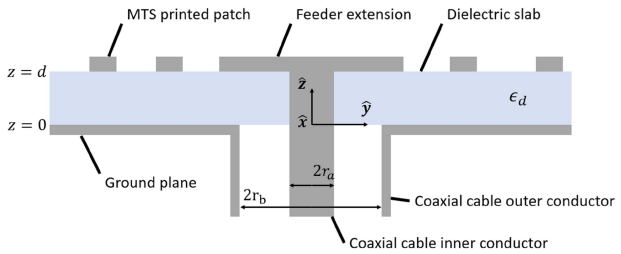

Fig. 1. Representation of the probe-fed MTS antenna. The metallic parts are modeled as 0-thickness perfect electric conductors.

geometry of the probe. Local basis functions [30] or harmonic basis functions can be used to describe the probe [31]. The main difficulties with this approach are the evaluation of Green's function [19], [20], [21] and the accurate treatment of the electrical connection between the probe and the horizontal conductor. The electrical connection between the probe and the patch is usually realized using an attachment mode [32], [33], [34], [35]. An attachment mode is a basis function simultaneously defined on both the probe and the patch. This basis function is used to enforce the current continuity across the intersection line between the outer surface of the probe and the patch surface. Two main types of attachment modes can be distinguished: the subdomain and entire-domain attachment modes. This description essentially characterizes the patch part. Regarding the subdomain attachment modes, the most popular one is probably the one given by [33], given its versatility versus different geometries and its spectral domain suitability. It is described as a radial current density spreading over a small fictitious disk concentric with the probe. Entire-domain attachment modes can be based, for example, on cavity model solutions [34]. It is shown in [35] that the subdomain attachment mode is in general more accurate and versatile than the entire-domain attachment mode. However, one uncertainty remains regarding the determination of the radius of the fictitious disk in the subdomain attachment mode.

Our modeling of the feeder is inspired by the approach proposed in [30]. In particular, the inner conductor of the coax feeder is meshed with rooftop basis functions, and broken (or bent) rooftops are used to model the transition between the vertical probe and the horizontal patch so as to enforce the current continuity at the air-dielectric interface. A Cartesian reference system of coordinates placed at the ground plane level and aligned with the probe axis is used (see Fig. 1). The cylindrical probe cross section is modeled as an octagon, and the current distribution along the surface of the probe is described with vertical rooftop basis functions as depicted in Fig. 2. The chosen octagonal cross section model results from a tradeoff between a limited number of basis functions and good accuracy. Bent rooftop basis functions are placed at the transition between the probe and the planar patch to ensure current continuity [30]. Half rooftop basis functions are placed on the bottom of the probe to establish the electrical connection with the ground plane. The planar patch is meshed with local basis functions (see Fig. 4). Details regarding the computation of the MoM impedance matrix are outside the scope of this article. The reader is referred to [32] and [36] for more details regarding the calculation of reaction integrals.

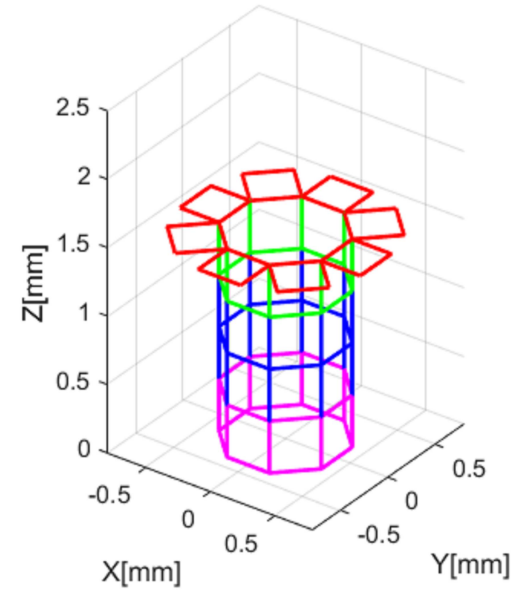

Fig. 2. Probe meshed with rooftop basis functions. Magenta half rooftop basis function ensure the connection with the ground plane. The rooftop basis functions in blue describe the current on the probe. Finally, the bent rooftops (each of them composed of a half vertical (green) and a half horizontal (red) rooftop basis function) ensure the current continuity at the air-dielectric interface.

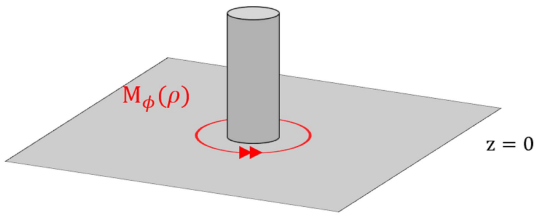

Fig. 3. Magnetic frill excitation scheme. The equivalence principle is used to model the electric field excitation at the bottom of the coax as an equivalent magnetic current distribution.

Since it is assumed that the coax line supports the propagation of the fundamental mode only, the electric field distribution on the coax section at $z = 0$ is a priori known. Resorting to the equivalence principle, this electric field distribution can be translated into an equivalent magnetic current distribution $\mathbf{M}$ on a perfect electric conductor (See Fig. 3). The magnetic current distribution serves as an excitation for the antenna, and is given by

$$\mathbf{M}(\rho) = \frac{-V}{2\rho \ln(r_b/r_a)}\hat{\boldsymbol{\phi}}, \qquad r_a \leq \rho \leq r_b, z = 0 \tag{1}$$

where V is the excitation voltage and $\rho = (x^2 + y^2)^{1/2}$ is the radial distance from the probe. This excitation is commonly called a magnetic frill excitation [37], [38]. The MoM excitation vector is obtained after testing the electric field generated by the magnetic frill with the vertical and horizontal basis functions [32].

The surface current distribution on the probe, and the planar patch is obtained after solving the resulting MoM system of equations. The input current I can be approximated by adding the MoM current coefficients of the bottom ($z = 0$; magenta) half rooftop basis functions depicted in Fig. 2 as follows:

$$I \approx \sum_{j=1}^{8} w_j \; i_{hr,j} \tag{2}$$

where w_j and $i_{hr,j}$ are the width and the current coefficient of the jth half rooftop basis functions connected to the ground plane, respectively. From there, the antenna input impedance can be estimated as $Z_{in} = I/V$ and the total active power delivered at the feed reads

$$P_{tot} = \Re\left(\frac{I^* V}{2}\right) \tag{3}$$

where $\Re$ and $*$ denote the real part and complex conjugate operators, respectively.

B. Validation of the Feeder Model

To validate the feeder model, a patch antenna is considered [see Fig. 4(a)] [29]. This patch is printed on a grounded dielectric slab of relative permittivity $2.22 - 0.0022$j, and thickness 1.52 mm. The inner, and outer radii of the coaxial conductors are chosen as $r_a = 0.43$ mm and $r_b = 1.4$ mm, respectively. Fig. 4(b) shows a comparison with the results obtained with the frequency domain solver of the CST software for the input impedance based on the previously described method. A truncated grounded dielectric substrate of dimensions $625 \times 625 \times 1.52$ mm is considered in the CST model. As can be seen, there is a very good agreement, illustrating the accuracy of the model. In Section III, this model is incorporated into the fast analysis tool presented in [17], in order to analyze the complete MTS, including its coupling with the feeder.

III. MoM Formulation for Coax-Fed MTSs

A. Description of the MoM Formulation

Let us first consider a MTS antenna structure whose top view is depicted in Fig. 5 and whose side view is schematically represented in Fig. 1. The feeder is composed of a probe, and a central patch disk, with eventually a ring slot. The dimensions of the patch, the ring slot thickness and radius can be tuned to match the antenna input impedance. Outside the feeder lies the MTS, which is modeled as a modulated electric sheet impedance $\underline{\underline{\mathbf{Z}}}_S$. This surface impedance is meshed with rooftop basis functions on a rectangular and regular lattice, as previously explained in [17]. In particular, the current distribution on the MTS $\mathbf{J}_{MS}$ is expanded as follows:

$$\mathbf{J}_{MS}(\boldsymbol{r}) = \sum_{n=1}^{N_{MS}} i_{MS,n} \; \boldsymbol{F}_{MS,n}(\boldsymbol{r}) \tag{4}$$

where $\boldsymbol{F}_{MS,n}$ corresponds to the nth rooftop basis function on the MTS, and $i_{MS,n}$ is the corresponding expansion coefficient to be determined. Note that, in order to account for the not necessarily rectangular shape of the MTS, some coefficients $i_{M,n}$ are set to zero, as explained in [17, Sec. III]. As explained in Section II-A, the current distribution on the surface of the feeder is also discretized with elementary basis functions, i.e.,

$$\mathbf{J}_{FD}(\boldsymbol{r}) = \sum_{n=1}^{N_{FD}} i_{FD,n} \; \boldsymbol{F}_{FD,n}(\boldsymbol{r}) \tag{5}$$

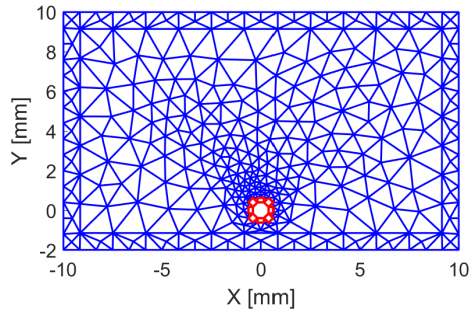

(a)

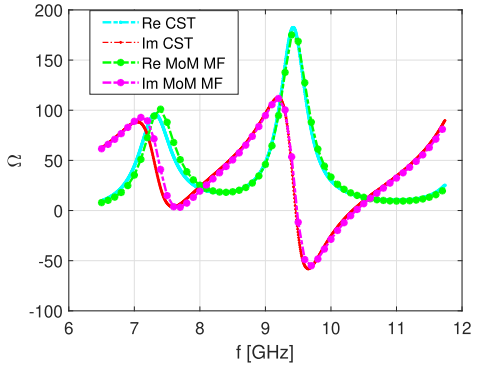

(b)

Fig. 4. Validation of the adopted feed model with CST. (a) Top-view of patch antenna. Hybrid basis functions are used at the transition between the broken rooftops of the feed and the RWG triangular basis functions of the patch. (b) Real and imaginary parts of the input impedance as a function of the frequency. Our results are compared with those from CST. MF indicates the magnetic frill excitation.

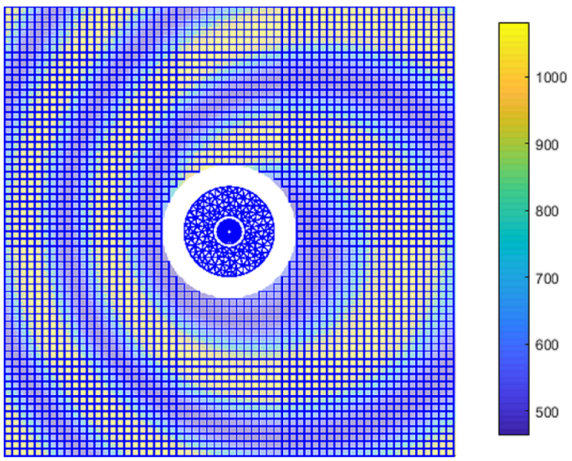

Fig. 5. Example of a meshed MTS antenna, including a realistic feeder. Absolute value of the xx component of the anisotropic sheet impedance given in (10).

where $\boldsymbol{F}_{FD,n}$ corresponds to a given elementary basis function on the feeder, which includes the rooftop basis functions of the probe, the Rao–Wilton–Glisson (RWG) basis functions for the planar metallization, and the hybrid basis functions for the transition between rooftop and RWG. Finally, the $i_{FD,n}$ scalars are the coefficients of expansion to be determined.

The MoM is used to find the surface current distribution on the MTS ($\mathbf{J}_{MS}$), and on the feeder ($\mathbf{J}_{FD}$), which translates into the determination of the unknown coefficients of expansion $i_{MS,n}$ and $i_{FD,n}$. To this end, the boundary conditions on the MTS and on the feeder should be enforced. On the MTS, the boundary condition to be satisfied is

$$\hat{\mathbf{n}} \times \left[\int\int_{S'} \underline{\underline{\mathbf{G}}}^{EJ}(\boldsymbol{r},\boldsymbol{r}') \left(\mathbf{J}_{MS}(\boldsymbol{r}') + \mathbf{J}_{FD}(\boldsymbol{r}')\right) \mathrm{d}S' - \underline{\underline{\mathbf{Z}}}_S(\boldsymbol{r})\, \mathbf{J}_{MS}(\boldsymbol{r}) \right] = -\hat{\mathbf{n}} \times \mathbf{E}_i^{MS} \quad (6)$$

where $\boldsymbol{r}$ and $\boldsymbol{r}'$ are positions vectors on the MTS, $\hat{\mathbf{n}}$ is the normal to the surface, $\underline{\underline{\mathbf{G}}}^{EJ}$ is the relevant dyadic GF of the grounded slab, and $\underline{\underline{\mathbf{Z}}}_S$ is the electric sheet impedance tensor. Finally, $\mathbf{E}_i^{MS}$ is the electric field generated on the MTS by the magnetic frill current. Similarly, the tangential electric field should vanish at the surface of the feed, i.e.,

$$\hat{\mathbf{n}} \times \left[\int\int_{S'} \underline{\underline{\mathbf{G}}}^{EJ}(\boldsymbol{r},\boldsymbol{r}') \left(\mathbf{J}_{MS}(\boldsymbol{r}') + \mathbf{J}_{FD}(\boldsymbol{r}')\right) \mathrm{d}S' \right] = -\hat{\mathbf{n}} \times \mathbf{E}_i^{FD} \quad (7)$$

where $\mathbf{E}_i^{FD}$ is the electric field generated on the surface of the feeder by the magnetic frill current. After inserting the current expansions (4) and (5) in (6) and (7), and testing the fields with the same basis functions (Galerkin testing), the following MoM system of equations matrix is obtained:

$$\begin{bmatrix} \mathbf{Z}_{MSMS} & \mathbf{Z}_{MSFD} \\ \mathbf{Z}_{MSFD}^T & \mathbf{Z}_{FDFD} \end{bmatrix} \begin{bmatrix} \mathbf{i}_{MS} \\ \mathbf{i}_{FD} \end{bmatrix} = \begin{bmatrix} \mathbf{v}_{MS} \\ \mathbf{v}_{FD} \end{bmatrix} \quad (8)$$

where $\mathbf{Z}_{MSMS}$ is the MTS impedance matrix given by [17, eqs. (3)–(5)], $\mathbf{Z}_{FDFD}$ is the feed impedance matrix as discussed in Section II-A, and the off-diagonal matrices contain the interactions between the feed and the MTS. $\mathbf{v}_{MS}$ and $\mathbf{v}_{FD}$ are fields from the magnetic frill excitation tested by the MTS and feed basis functions, respectively. Using the technique developed in [17, Sec. III], a system of equations involving only the MTS matrix $\mathbf{Z}_{MSMS}$ can be rapidly solved. Unfortunately, here, due to the inclusion of the feeder, and its coupling with the MTS, it is not possible to use the same technique to solve the system of equations in (8). Therefore, (8) is solved with the Schur complement method. First, the current $\mathbf{i}_{FD}$ on the feeder is computed by solving the following system of equations:

$$\left(-\mathbf{Z}_{MSFD}^T\, \mathbf{Z}_{MSMS}{}^{-1}\, \mathbf{Z}_{MSFD} + \mathbf{Z}_{FDFD}\right) \mathbf{i}_{FD} = \mathbf{v}_{FD} - \mathbf{Z}_{MSFD}^T\, \mathbf{Z}_{MSMS}{}^{-1}\, \mathbf{v}_{MS}. \quad (9)$$

This equation is solved iteratively using the generalized minimal residual method (GMRES) technique [39]. At each iteration, the matrix-vector multiplication with $\mathbf{Z}_{MSMS}^{-1}$ is also computed iteratively using the method presented in [17]. Note that the number of iterations required to solve (9) can be dramatically reduced if the inverse of the feeder self-interaction matrix $\mathbf{Z}_{FDFD}$ is used as a preconditioner. To analyze that preconditioning effect, we consider a square MTS antenna of size $3\lambda_0 \times 3\lambda_0$, lying on a substrate with relative permittivity 3.66 and thickness 1.524 mm.

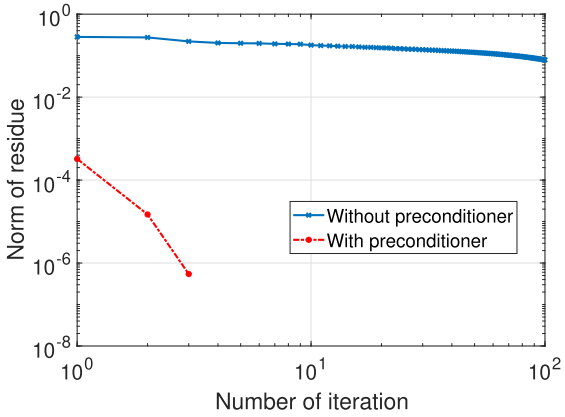

Fig. 6. GMRES convergence for the system of equations (9) considering the MTS in Fig. 5.

The sheet impedance modeling MTS is given by [10]

$$\begin{aligned} Z^{\rho\rho} &= jX_0[1 + M\cos(k_{sw}\rho - k_0\rho\sin\theta_0\cos\phi - \phi)] \\ Z^{\rho\phi} &= Z^{\phi\rho} = jX_0 M\sin(k_{sw}\rho - k_0\rho\sin\theta_0\cos\phi - \phi) \\ Z^{\phi\phi} &= jX_0[1 - M\cos(k_{sw}\rho - k_0\rho\sin\theta_0\cos\phi - \phi)] \end{aligned} \quad (10)$$

with $X_0 = -772\ \Omega$ being the average reactance. $M = 0.4$ is the modulation depth, $k_{sw} = 1.35\ k_0$ is the supported SW wavenumber, and $(\theta_0 = 0)$ is the radiating direction, here at broadside. (ρ, ϕ) are the classical polar coordinates, with the origin at the center of the MTS. The convergence of GMRES (with and without preconditioning) is plotted in Fig. 6. It can be observed that preconditioning with the inverse of the feeder self-interaction matrix dramatically accelerates the convergence. This is due to the relatively small backward coupling between the MTS and the feeding structure.

Once the coefficients for currents on the feed $\mathbf{i}_{FD}$ are obtained, the current coefficients on the MTS $\mathbf{i}_{MTS}$ are derived as

$$\mathbf{Z}_{MSMS}\ \mathbf{i}_{MS} = (\mathbf{v}_{MS} - \mathbf{Z}_{MSFD}\ \mathbf{i}_{FD}). \quad (11)$$

Equation (11) can be rapidly solved using the technique described in [17, Sec. III].

B. Validation of the Vertical Probe Model With the FBBF-Based Method

The vertical probe model is validated with the Fourier–Bessel-based tool presented in [40]. In the latter, entire-domain basis functions called Fourier–Bessel basis functions (FBBF) have been used to analyze circular MTSs, and the feeder has been modeled by a vertical infinitesimal dipole. We consider a circular MTS of radius $7.5\lambda_0$, with λ_0 being the free-space wavelength. The impedance profile, and the substrate are the same as the ones considered in Section III-A. This antenna is designed to radiate a circularly polarized broadside beam. For comparison with the model of [40], the feeder is simply constituted of a vertical probe (a pin as shown in Fig. 3) with radius 0.2 mm. The radius of the coaxial cable outer conductor is 0.475 mm and the MTS covers the whole circular aperture of the antenna. Fig. 7 shows the evolution of the aperture efficiency (ϵ_{ap}), the conversion efficiency (ϵ_{conv}) and the total efficiency ($\epsilon = \epsilon_{ap} \times \epsilon_{conv}$) as a function on the modulation depth M of the impedance distribution.

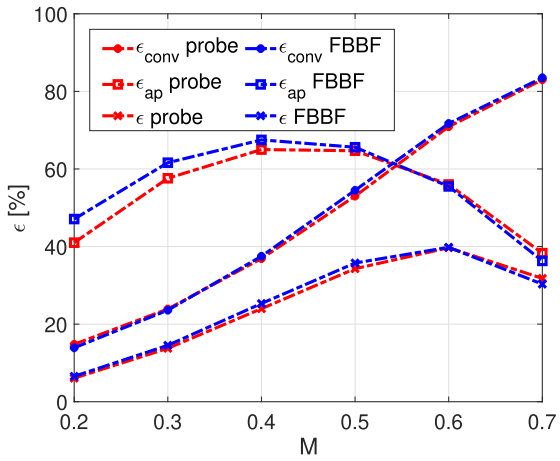

Fig. 7. Comparison of the vertical probe model with the infinitesimal dipole model from [40]. The efficiencies of the antenna, computed with both approaches are compared.

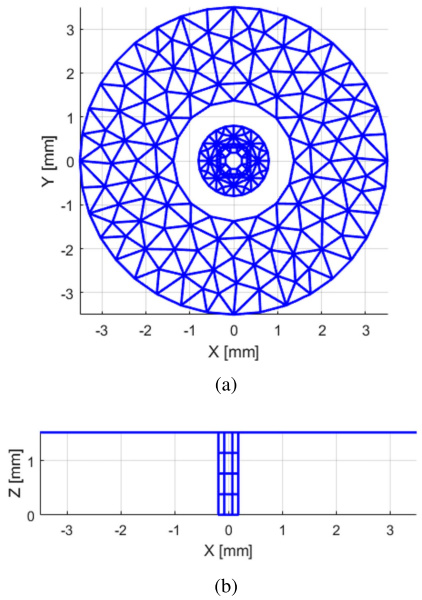

Fig. 8. Feeder structure and mesh. (a) Top view. (b) Side view.

As can be observed, although the two methods are based on different basis functions and feeder models, a good agreement is observed between the two formulations for total efficiency.

C. Impact of the Full-Wave characterization of the Feeder

Now, let us analyze the impact of introducing a more realistic feeder. To this end, a hole of $0.5\lambda_0$ radius has been made in the center of the MTS and we have added a circular ring patch (represented in Fig. 8) on top of the probe. This patch is composed of an inner disk of radius 0.8 mm, a gap of size 0.575 mm, and a ring with an outer radius of 3.5 mm. Those feeder dimensions have been chosen to match the antenna at 50 Ω at 24 GHz. Efficiency results previously obtained without a patch disk on top of the probe are compared with those obtained with the patch disk (i.e., with a full-wave

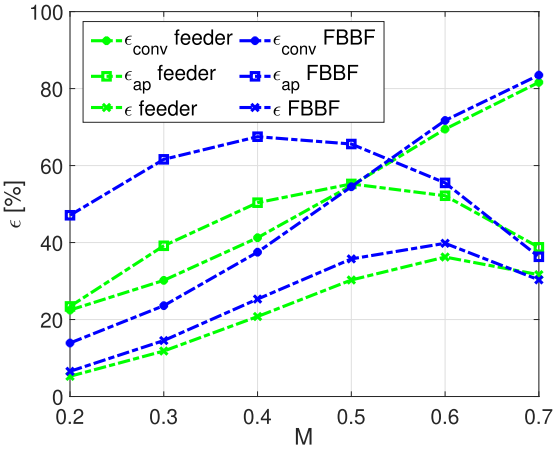

(a)

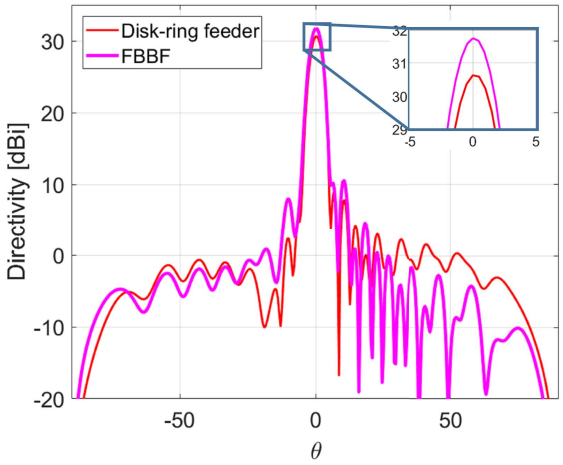

(b)

Fig. 9. Comparison between the FBBF-based method, modeling the feed as a point source and the proposed method, fully characterizing the feed as shown in Fig. 8. (a) Efficiency results as a function of the modulation depth. (b) Co-polar directivity.

modeling of the feed) in Fig. 9(a). The directivity pattern in the $\phi = 0$ plane, and for $M = 0.4$ is shown in Fig. 9(b).

It is interesting to see that the full-wave feeder modeling introduces some variations on the aperture and conversion efficiencies and impacts the sidelobes level of the radiation pattern. The differences observed are stronger when looking individually at the conversion and aperture efficiencies than when looking at the total efficiency. For example, there is a 2 dB difference on the directivity between the two models at $M = 0.3$, and 1.3 dB difference at $M = 0.4$. These comparisons highlight the importance of accounting for the geometry of the feeding structure, in particular when one needs to control accurately the sidelobes.

D. Analysis of the Coupling Between the Feeder and the MTS

This section analyzes the impact of the coupling feed-MTS, on the antenna input impedance. For this purpose, we have computed the input impedance of the antenna described in Section III-A in three different cases. The first case corresponds to the feed, with top disk included, laying on the

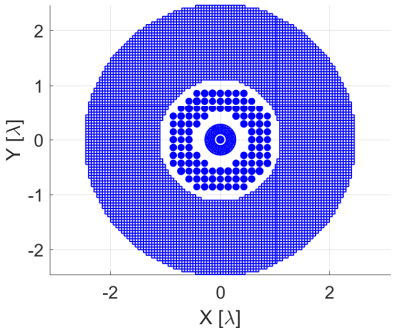

(a)

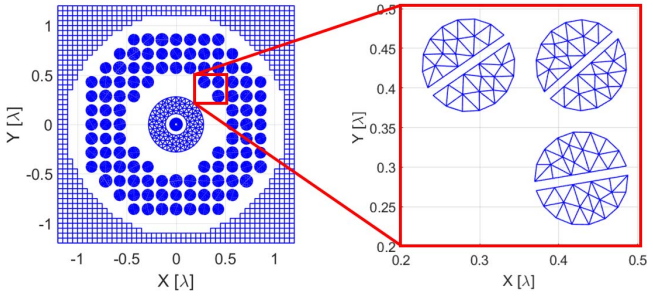

(b)

Fig. 10. $2.5\lambda_0$ radius MTS antenna described with both sheet impedance model and coffee bean patches. (a) Global view. (b) Central zoom.

infinite slab, and without the presence of MTS. In the second case, we have added the sheet impedance distribution around the feed, and the antenna radius has been fixed to 2.5λ. In the third case, the portion of the MTS close to the feed has been implemented with coffee bean patches. These have been designed to implement the desired surface impedance in the inner part of the MTS, i.e., radius $\in [0.5\lambda_0,\ \lambda_0]$) (see Fig. 10).

Fig. 11 shows the input impedance and the reflection coefficient as a function of the frequency. One can conclude that the presence of the MTS around the feed does not strongly affect the matching of the antenna. That means the antenna matching can be carried out almost independently of the MTS design.

E. Computational Speed of the Method

This section provides the computational performance of the method, in the presence (or not) of a top disk feeder. The top disk and the probe have been meshed with 476, and 32 basis functions, respectively. The simulations are carried out using a single computer equipped with an Intel Core i5-7500 CPU with a 3.4 GHz clock and 24 GB of RAM. The simulation time is evaluated considering a circular MTS described with the surface impedance given by (10) and the same substrate as in Section III-A. The feeder is fully meshed, as sketched in Fig. 8. An overview of the simulation time for each step is given in Table I.

As can be seen, the most expensive steps in terms of simulation time and memory are the filling of $\mathbf{Z}_{MSFD}$, the filling of $\mathbf{Z}_{FDFD}$, and the excitation vector calculation. However, when one needs to optimize the MTS sheet at a given frequency

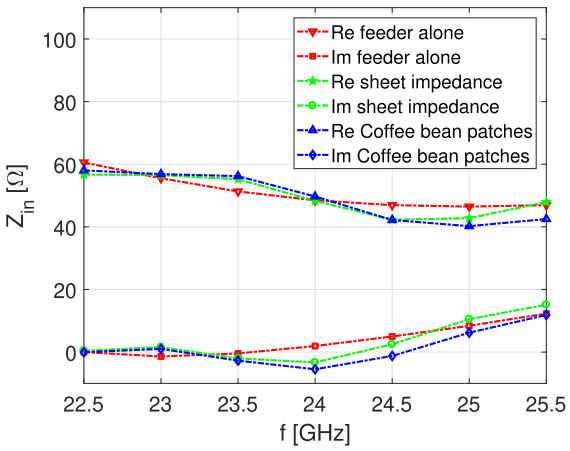

(a)

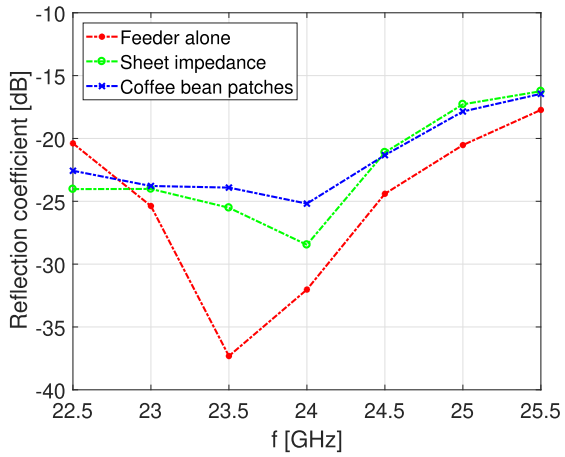

(b)

Fig. 11. Input impedance: feeder alone versus feeder surrounded by MTS modeled as sheet impedance versus feeder surrounded by MTS, including coffee bean patches (see Fig. 10).

of operation, with a given substrate, those calculations have to be made only once. As a consequence, the MTS antenna can be rapidly optimized, while fully modeling the feeder. This feature is exploited hereafter to optimize the efficiency of MTS antennas, and/or to control the sidelobes level.

IV. Far-Field Optimization of MTS Antennas

Let us assume that one needs to design a MTS radiating a pencil beam pointing in an arbitrary direction. For a circular polarization, the required impedance profile has been derived in [10], and is given by (10). In that expression, the modulation index and the supported SW wavenumber should be chosen/optimized to achieve a maximum efficiency. A simple optimization procedure based on the previously described method is proposed in this section to guide the user toward the rapid optimization of the MTS antenna, and avoid reaching non-desired local minima. Contrary to the approaches developed in [14], [15], and [16], here the feeder is fully analyzed as well as its coupling with the MTS and the proposed algorithm enables the reduction of the sidelobe level.

TABLE I

Evaluation Time of the Method Proposed in Section III-E

MTS antenna radius	7.5 λ_0	10 λ_0	12.5 λ_0	15 λ_0
Number of unknowns	138940	248236	389020	561172
$\mathbf{Z}_{FDFD}$ filling time [min]	6	6	6	6
$\mathbf{Z}_{MSFD}$ filling time [min]	49	90	143	208
Excitation vector $\mathbf{v}$ computation time [min]	0.93	1.45	1.97	2.64
$\mathbf{Z}_{MSMS}$ filling time [min]	0.29	0.54	0.9	1.3
Solving time using Schur's complement [min]	0.32	0.78	2.04	4

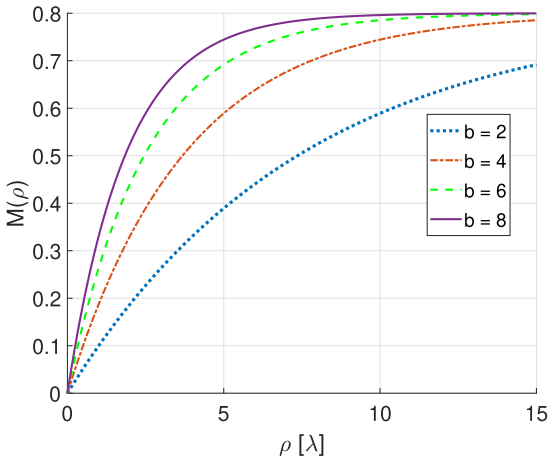

Fig. 12. Illustration of the nonuniform modulation index, considering $a = 0.8$ and different values of b.

A. Optimization of the Efficiency of MTS Antennas

1) Description of the Algorithm: It has been shown in [40], [41], [42], and [11] that a nonuniform modulation index $M(\rho)$, can lead to a higher efficiency, as compared to the uniform modulation. Intuitively, increasing the modulation index when moving from the center of the antenna to the rim can enable the compensation of the progressive attenuation of the SW due to radiation, so as to maintain a quasi-uniform radiating power density over the aperture. In this way, one can reach a high aperture efficiency without sacrificing the conversion efficiency, thus maximizing the overall efficiency.

In this work, we propose the following nonuniform model for the modulation index:

$$M(\rho) = a\left(1 - \mathrm{e}^{-b\rho/\rho_{max}}\right) \tag{12}$$

where ρ_{max} is the antenna maximum spatial extent from the origin and the parameters a and b are tuned to optimize the antenna efficiency. More specifically, a imposes the maximum value of $M(\rho)$ and b controls the convergence rate. An example of this model is depicted in Fig. 12.

Since the supported wavenumber k_{sw} depends on the modulation index, an optimized design will require the local computation of k_{sw}. However, we have observed that a well-chosen constant value of k_{sw} is sufficient to achieve an excellent performance. It should be noted that the method

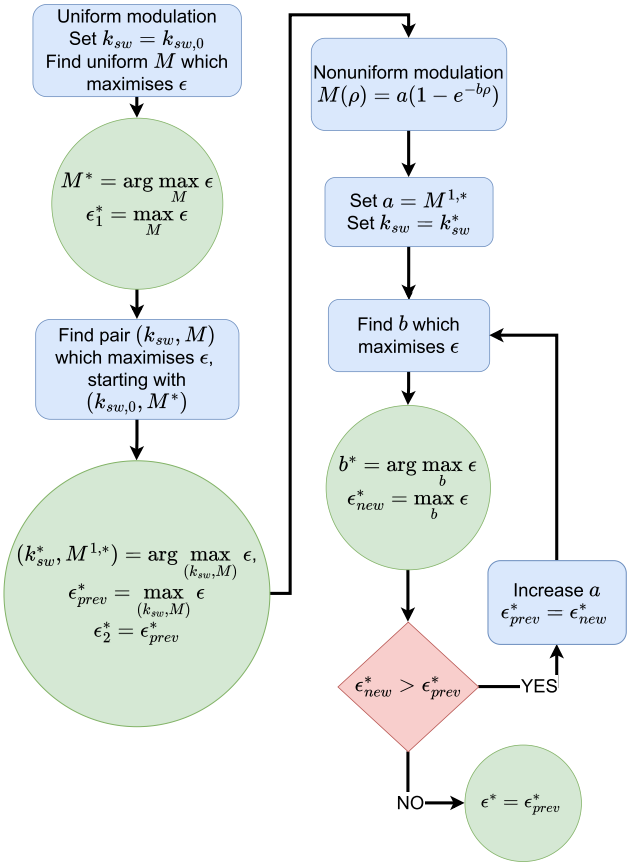

Fig. 13. Optimization algorithm for MTS efficiency.

TABLE II

EFFICIENCY OBTAINED FOR CIRCULAR MTS USING THE OPTIMIZATION ALGORITHM IN FIG. 13

MTS antenna radius	7.5 λ_0	10 λ_0	12.5 λ_0	15 λ_0
ϵ^*[%]	59.1	62.2	66.4	69.2
ϵ_{conv}^*[%]	82.6	85	89.4	94.7
ϵ_{ap}^*[%]	71.6	73.2	74.3	73
Parameter a	0.75	0.69	0.7	0.8
Parameter b	5.53	5.25	4.28	2.9
k_{sw}^*	$k_{sw,0}/0.96$	$k_{sw,0}/0.97$	$k_{sw,0}/0.97$	$k_{sw,0}/0.965$
ϵ_1^*[%]	39	37.5	38	37
ϵ_2^*[%]	53.3	53.2	53.3	53.5

enables a more elaborated modeling of k_{sw}. The optimization algorithm is illustrated in Fig. 13. First the supported SW mode is computed as the one corresponding to the average reactance, i.e., in the absence of modulation ($k_{sw,0}$ [44]). A uniform modulation index M is then assumed, and tuned to maximize the antenna efficiency. Then, starting from the previously obtained pair ($k_{sw,0}$, M^*), the SW wavenumber and the uniform modulation index are tuned simultaneously to optimize the efficiency. The resulting solution (k_{sw}^*, $M^{1,*}$) constitutes the optimized design for a uniform modulation index.

In the second part of the algorithm, the parameters a and k_{sw} are set to the values $M^{1,*}$, k_{sw}^*, previously obtained. After that, b is tuned to maximize the efficiency. If the resulting efficiency is higher than the previous one, the value of a is increased. However, if the previous efficiency is higher than the new one, the previous efficiency is selected as the optimized one. After this step, a better efficiency may sometimes be obtained by tuning again k_{sw}.

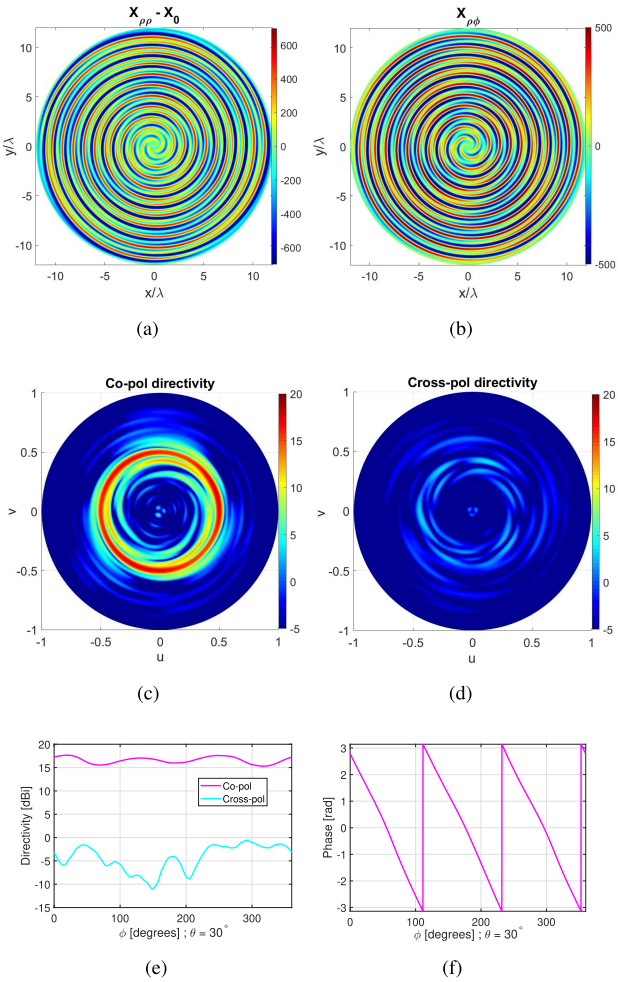

Fig. 14. Conical beam with OAM. (a) $\rho\rho$ component of the reactance modulation. (b) $\rho\phi$ component of the reactance modulation. (c) and (d) Directivity cut in the uv plane. (e) Amplitude of the directivity in the cone $\theta = 30°$. (f) Phase of the directivity in the cone $\theta = 30°$.

2) Optimization of the Efficiency of a Circular MTS Radiating a Broadside Pencil Beam: We consider a circular MTS antenna radiating a circularly polarized broadside beam, with a substrate with relative permittivity $\epsilon_r = 3.66$, and thickness $d = 1.524$ mm. The overall efficiency has been optimized with the previously described algorithm. The results are shown for different MTS radii in Table II. The intermediate results ϵ_1^*, ϵ_2^* are also provided.

One can conclude that the achievable optimum efficiency varies with respect to the antenna radius. The optimized efficiency increases with the antenna radius up to a maximum; here approximately (70%). Comparing ϵ_1^*, ϵ_2^*, and ϵ, it can be concluded that the optimization of k_{sw}, and M, is required to achieve a maximum performance. Exceeding 70% efficiency will require a proper design of the feed so as to minimize the space waves directly radiated by the feeder.

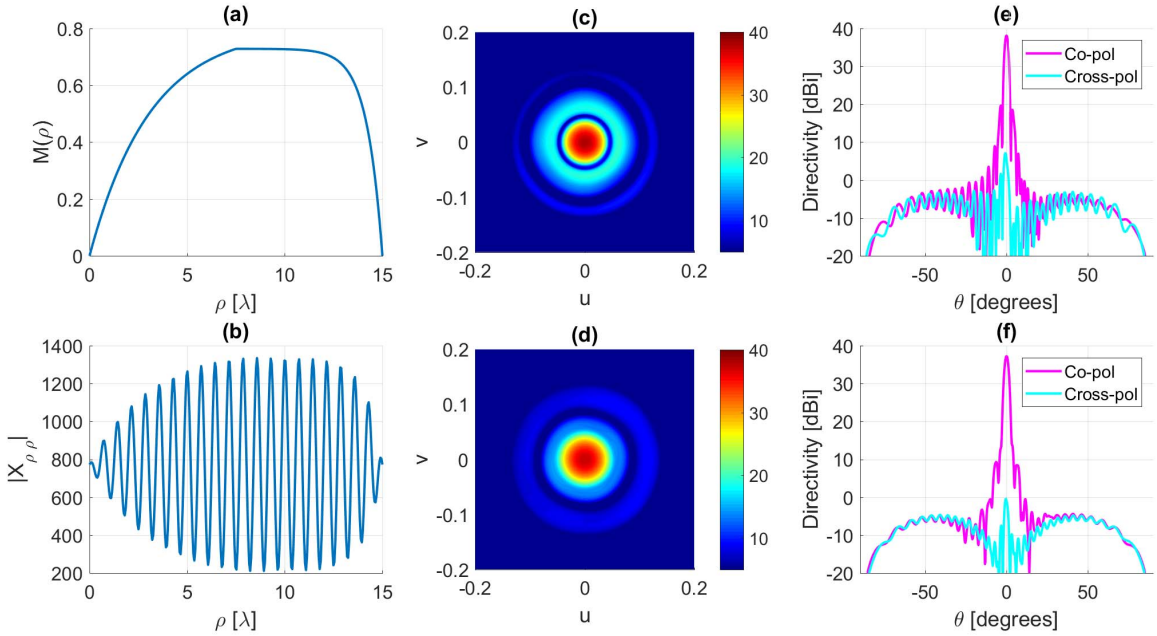

Fig. 15. Optimization of the sidelobe level. (a) Index modulation $M(\rho)$. (b) Sheet impedance modulation $X_{\rho\rho}$. (c) Co-polar directivity when the efficiency is optimized without considering the sidelobe level. (d) Co-polar directivity when the efficiency and the sidelobe level are optimized simultaneously. (e) and (f) Directivity pattern cut in the highest sidelobe plane, considering the solution without and with sidelobe optimization, respectively.

3) Optimization of the Efficiency of a Circular MTS Radiating a Conical Beam With OAM: This section provides optimization results for a MTS antenna radiating a circularly polarized conical beam pointing at $\theta = 30°$, with orbital angular momentum (OAM), i.e., with a phase linearly evolving along azimuth [45]. Contrary to MTS antennas radiating pencil beams, an analytical expression of the surface impedance required for such beams does not exist in the literature. Therefore, we have designed the MTS with the integral-equation-based method proposed in [12], and the modulation depth of the obtained solution has been optimized with the method presented in Section IV-A. The optimization has been carried out while fully modeling the feed. Note that, here, the parameter k_{sw} has not been optimized. The results are shown in Fig. 14 for a MTS with 12λ radius. We obtained a conversion efficiency of 85.66%, with an average directivity equal to 16.5 dBi in the radiating cone ($\theta = 30°$). It is worth mentioning that multiplexing information with OAM beams is limited to the near-field because of the faster on-axis decay of OAM beams [45].

B. Optimization of the Efficiency of a Rectangular MTS

An advantage of the proposed MTS modeling is that it can be used for arbitrarily shaped MTSs. For example, we have optimized a rectangular shaped MTS antenna of dimension $17\lambda_0 \times 10\lambda_0$, radiating a cicularly polarized broadside beam with the same substrate as before. For this example, we have obtained a = 0.72 and b = 9.4, leading to an an aperture efficiency of 68%, a conversion efficiency of 74%, and a compound efficiency of 50.3%. For comparison, a circular MTS antenna with comparable area, i.e., with a $7.5\lambda_0$ radius, provides a 59.1% efficiency. That means, better results are obtained with a circular antenna. The optimization of the rectangular shaped antenna may be improved by introducing an azimuthal dependence of the optimized modulation index, and the supported SW wavenumber. The incorporation of this azimuthal asymmetry in the optimization algorithm is straightforward.

V. Sidelobe Level Reduction

Section IV has dealt with the optimization of the antenna efficiency. In some applications, the antenna efficiency may not be the only constraint. For example, a radar antenna may require a very low sidelobe level to avoid clutter detection. From Section IV-A2, the optimized circular MTS antenna of radius $15\lambda_0$ provides an efficiency of 69.2%, with a sidelobe level 18.45 dB lower than the main lobe [see Fig. 15(e)]. One may prefer to reduce the sidelobe level at the expense of a lower efficiency. The sidelobe level mainly results from the diffraction effect due to the radiating field discontinuity at the MTS edge. That means, controlling the sidelobe level requires a progressive diminution of the power radiated close to the MTS edge, which translates into a progressive diminution of the modulation index. Therefore, the following extended model for the modulation index is proposed:

$$\begin{aligned} M(\rho) &= a\left(1 - \mathrm{e}^{-b\rho/\rho_{max}}\right), \qquad \rho \le c \\ M(\rho) &= M_{max} - a_2\left(1 - \mathrm{e}^{b_2(\rho - c)}\right), \qquad \rho > c \end{aligned} \tag{13}$$

where $\rho = c$ is the radius at which the modulation index is maximum [i.e., $M_{max} = M(c)$], and $a_2 = M_{max}/(1 - \mathrm{e}^{b_2(\rho_{max} - c)})$. The expression of a_2 ensures the continuity of $M(\rho)$ at the transition point ($\rho = c$). a–c, and b_2 are the optimization variables, and ρ_{max} is the antenna radius.

Parameter c controls the radius at which the modulation index starts decreasing, and parameter b_2 controls the decaying slope. The objective function is now defined as

$$F = \epsilon_{conv}\epsilon_{ap}\epsilon_{sl}^2 \tag{14}$$

with ϵ_{sl} being the ratio between the main lobe level and the maximum sidelobe level. The square on top of ϵ_{sl} is used to put more weight on the sidelobe level reduction. Other rules may be used to combine the different figures of merit. The optimization is carried out on a MTS of radius $15\lambda_0$, with a procedure similar to the one described in the previous section. The modulation index and sheet impedance modulation maximizing F are shown in Fig. 15(a) and (b). The resulting radiation pattern (in the uv plane) is represented in Fig. 15(d), and compared with the one obtained from the efficiency optimization [see Fig. 15(c)]. The directivity cuts along the highest sidelobe plane resulting from the efficiency optimization without and with sidelobe minimization are respectively shown in Fig. 15(e) and (f). It can be observed that the sidelobe level is now lower (28 dB below the main beam). In comparison, when the optimization was carried out on the antenna efficiency only, the sidelobe level was 18.4 dB lower. However, the improvement of the sidelobe level has been obtained at the expense of a lower aperture efficiency (73% versus 59.7%).

VI. Conclusion

Optimizing MTS antennas while fully modeling the feeder is required when one needs a fine control of the antenna directivity (less than 2 dB error). However such optimization is a complex task because of the required meticulous treatment of the underlying Green's functions, reaction integrals and attachment modes. A detailed analysis and optimization of coax-fed MTS antennas has been presented. First a model of the probe is provided and validated considering a printed patch antenna. Then, the probe model is combined with a recent algorithm developed to rapidly analyze arbitrarily shaped MTSs [17]. The resulting method enables a rapid optimization of the MTS antenna far-field pattern, while fully modeling the feeder. This allows one to establish a proper trade-off between conversion efficiency, directivity and sidelobe level, while also ensuring a good impedance matching. In addition, it has been shown based on a practical example that the matching of the antenna can be carried out by tuning the feeder dimensions, while ignoring the presence of the MTS. Further works should include the full-wave modeling of the fine geometry of the MTS patches, so as to accurately predict the antenna radiation prior to fabrication.

References

[1] O. Quevedo-Teruel et al., "Roadmap on metasurfaces," *J. Opt.*, vol. 21, no. 7, 2019, Art. no. 073002.

[2] B. Assouar, B. Liang, Y. Wu, Y. Li, J.-C. Cheng, and Y. Jing, "Acoustic metasurfaces," *Nature Rev. Mater.*, vol. 3, no. 12, pp. 460–472, 2018.

[3] C. L. Holloway, A. Dienstfrey, E. F. Kuester, J. F. O'Hara, A. K. Azad, and A. J. Taylor, "A discussion on the interpretation and characterization of metafilms/metasurfaces: The two-dimensional equivalent of metamaterials," *Metamaterials*, vol. 3, no. 2, pp. 100–112, 2009.

[4] L. Liang and S. V. Hum, "Design of a UWB reflectarray as an impedance surface using Bessel filters," *IEEE Trans. Antennas Propag.*, vol. 64, no. 10, pp. 4242–4255, Oct. 2016.

[5] M. Di Renzo et al., "Smart radio environments empowered by reconfigurable intelligent surfaces: How it works, state of research, and the road ahead," *IEEE J. Sel. Areas Commun.*, vol. 38, no. 11, pp. 2450–2525, Nov. 2020.

[6] C. Pfeiffer and A. Grbic, "Metamaterial Huygens' surfaces: Tailoring wave fronts with reflectionless sheets," *Phys. Rev. Lett.*, vol. 110, May 2013, Art. no. 197401.

[7] N. Mohammadi Estakhri and A. Alù, "Wave-front transformation with gradient metasurfaces," *Phys. Rev. X*, vol. 6, no. 4, Oct. 2016.

[8] A. Epstein and G. V. Eleftheriades, "Synthesis of passive lossless metasurfaces using auxiliary fields for reflectionless beam splitting and perfect reflection," *Phys. Rev. Lett.*, vol. 117, no. 25, Dec. 2016, Art. no. 256103.

[9] B. H. Fong, J. S. Colburn, J. J. Ottusch, J. L. Visher, and D. F. Sievenpiper, "Scalar and tensor holographic artificial impedance surfaces," *IEEE Trans. Antennas Propag.*, vol. 58, no. 10, pp. 3212–3221, Oct. 2010.

[10] G. Minatti et al., "Modulated metasurface antennas for space: Synthesis, analysis and realizations," *IEEE Trans. Antennas Propag.*, vol. 63, no. 4, pp. 1288–1300, Apr. 2015.

[11] M. Faenzi et al., "Metasurface antennas: New models, applications and realizations," *Sci. Rep.*, vol. 9, no. 1, pp. 1–14, Dec. 2019.

[12] M. Bodehou, C. Craeye, E. Martini, and I. Huynen, "A quasi-direct method for the surface impedance design of modulated metasurface antennas," *IEEE Trans. Antennas Propag.*, vol. 67, no. 1, pp. 24–36, Jan. 2019.

[13] A. Amini, H. Oraizi, M. Hamedani, and A. Keivann, "Wide-band polarization control of leaky waves on anisotropic holograms," *Phys. Rev. Appl.*, vol. 13, Jan. 2020, Art. no. 014038.

[14] D. González-Ovejero and S. Maci, "Gaussian ring basis functions for the analysis of modulated metasurface antennas," *IEEE Trans. Antennas Propag.*, vol. 63, no. 9, pp. 3982–3993, Sep. 2015.

[15] M. Bodehou, D. González-Ovejero, C. Craeye, and I. Huynen, "Method of moments simulation of modulated metasurface antennas with a set of orthogonal entire-domain basis functions," *IEEE Trans. Antennas Propag.*, vol. 67, no. 2, pp. 1119–1130, Feb. 2019.

[16] F. Vernìì, M. Righero, and G. Vecchi, "On the use of entire-domain basis functions and fast factorizations for the design of modulated metasurface," *IEEE Trans. Antennas Propag.*, vol. 68, no. 5, pp. 3824–3833, May 2020.

[17] J. Cavillot, M. Bodehou, S. Hubert, and C. Craeye, "Efficient analysis of planar, arbitrarily shaped, and (Bi)-anisotropic metasurface antennas," *IEEE Trans. Antennas Propag.*, vol. 70, no. 1, pp. 536–546, Jan. 2022.

[18] *Computer Simulation Technology (CST)*. Accessed: Nov. 15, 2021. [Online]. Available: https://www.3ds.com/fr/produits-et-services/simulia/produits/cst-studio-suite/

[19] J. R. Mosig and F. E. Gardiol, "Analytical and numerical techniques in the Green's function treatment of microstrip antennas and scatterers," *IEE Proc. H (Microw., Opt. Antennas)*, vol. 130, no. 2, pp. 175–182, Mar. 1983.

[20] N. K. Das and D. M. Pozar, "A generalized spectral-domain Green's function for multilayer dielectric substrates with application to multilayer transmission lines," *IEEE Trans. Microw. Theory Techn.*, vol. MTT-35, no. 3, pp. 326–335, Mar. 1987.

[21] K. A. Michalski and J. R. Mosig, "Multilayered media Green's functions in integral equation formulations," *IEEE Trans. Antennas Propag.*, vol. 45, no. 3, pp. 508–519, Mar. 1997.

[22] M. Davidovitz and Y. T. Lo, "Input impedance of a probe-fed circular microstrip antenna with thick substrate," *IEEE Trans. Antennas Propag.*, vol. AP-34, no. 7, pp. 905–911, Jul. 1986.

[23] N. Kinayman and M. I. Aksun, "Efficient use of closed-form Green's functions for the analysis of planar geometries with vertical connections," *IEEE Trans. Microw. Theory Techn.*, vol. 45, no. 5, pp. 593–603, May 1997.

[24] M. Vrancken and G. A. E. Vandenbosch, "Hybrid dyadic-mixed-potential and combined spectral-space domain integral-equation analysis of quasi-3-D structures in stratified media," *IEEE Trans. Microw. Theory Techn.*, vol. 51, no. 1, pp. 216–225, Jan. 2003.

[25] G. Valerio et al., "Efficient computation of 1-D periodic layered mixed potentials for the analysis of leaky-wave antennas with vertical elements," *IEEE Trans. Antennas Propag.*, vol. 63, no. 6, pp. 2396–2411, Jun. 2015.

[26] K. Carver and J. Mink, "Microstrip antenna technology," *IEEE Trans. Antennas Propag.*, vol. AP-29, no. 1, pp. 2–24, Jan. 1981.

[27] W. Richards, Y. Lo, and D. Harrison, "An improved theory for microstrip antennas and applications," *IEEE Trans. Antennas Propag.*, vol. AP-29, no. 1, pp. 38–46, Jan. 1981.
[28] D. M. Pozar, "Input impedance and mutual coupling of rectangular microstrip antennas," *IEEE Trans. Antennas Propag.*, vol. AP-30, no. 6, pp. 1191–1196, Nov. 1982.
[29] R. C. Hall and J. R. Mosig, "The analysis of coaxially fed microstrip antennas with electrically thick substrates," *Electromagnetics*, vol. 9, no. 4, pp. 367–384, Jan. 1989.
[30] T. M. Grzegorczyk and J. R. Mosig, "Line charge distributions arising in the integral equation treatment of bent scatterers in stratified media," *IEE Proc.-Microw., Antennas Propag.*, vol. 148, no. 6, pp. 365–368, Dec. 2001.
[31] R. Rodriguez-Berral, F. Mesa, and D. R. Jackson, "Excitation of an infinite microstrip line with a vertical coaxial feed," *IEEE Trans. Microw. Theory Techn.*, vol. 56, no. 7, pp. 1638–1648, Jul. 2008.
[32] A. B. Smolders, "Microstrip phased-array antennas: A finite-array approach," Ph.D. dissertation, Fac. Elect. Eng., Technische Universiteit Eindhoven, Eindhoven, The Netherlands, 1994.
[33] S. Pinhas, S. Shtrikman, and D. Treves, "Moment-method solution of the center-fed microstrip disk antenna invoking feed and edge current singularities," *IEEE Trans. Antennas Propag.*, vol. 37, no. 12, pp. 1516–1522, Dec. 1989.
[34] J. T. Aberle and D. M. Pozar, "Analysis of infinite arrays of probe-fed rectangular microstrip patches using a rigorous feed model," *Proc. Inst. Elect. Eng.*, vol. 136, no. 2, pp. 110–119, Apr. 1989.
[35] G. Mayhew-Ridgers, J. W. Odendaal, and J. Joubert, "Entire-domain versus subdomain attachment modes for the spectral-domain method of moments analysis of probe-fed microstrip patch antennas," *IEEE Trans. Antennas Propag.*, vol. 52, no. 6, pp. 1616–1620, Jun. 2004.
[36] J. Cavillot, "Fast electromagnetic analysis of large objects involving planar layered media: Application to antenna arrays and metasurfaces," Ph.D. dissertation, Inst. Inf. Commun. Technol., Electron. Appl. Math. (ICTEAM), UCLouvain, Ottignies-Louvain-la-Neuve, Belgium, 2021.
[37] L. Tsai, "A numerical solution for the near and far fields of an annular ring of magnetic current," *IEEE Trans. Antennas Propag.*, vol. AP-20, no. 5, pp. 569–576, Sep. 1972.
[38] C. M. Butler and L. Tsai, "An alternate frill field formulation," *IEEE Trans. Antennas Propag.*, vol. AP-21, no. 1, pp. 115–116, Jan. 1973.
[39] Y. Saad and M. H. Schultz, "GMRES: A generalized minimal residual algorithm for solving nonsymmetric linear systems," *SIAM J. Sci. Statist. Comput.*, vol. 7, no. 3, pp. 856–869, 1986.
[40] M. Bodehou, D. González-Ovejero, C. Craeye, S. Maci, I. Huynen, and E. Martini, "Power balance and efficiency of metasurface antennas," *Sci. Rep.*, vol. 7, p. 17508, Oct. 2020.
[41] G. Minatti, E. Martini, and S. Maci, "Efficiency of metasurface antennas," *IEEE Trans. Antennas Propag.*, vol. 65, no. 4, pp. 1532–1541, Apr. 2017.
[42] G. Minatti, M. Faenzi, M. Sabbadini, and S. Maci, "Bandwidth of gain in metasurface antennas," *IEEE Trans. Antennas Propag.*, vol. 65, no. 6, pp. 2836–2842, Jun. 2017.
[43] M. Faenzi et al., "Metasurface antennas: New models, applications and realizations," *Sci. Rep.*, vol. 9, no. 1, pp. 1–14, Dec. 2019.
[44] G. Minatti, F. Caminita, E. Martini, and S. Maci, "Flat optics for leaky-waves on modulated metasurfaces: Adiabatic floquet-wave analysis," *IEEE Trans. Antennas Propag.*, vol. 64, no. 9, pp. 3896–3906, Sep. 2016.
[45] M. Tamagone, C. Craeye, and J. Perruisseau-Carrier, "Encoding many channels on the same frequency through radio vorticity: First experimental test," *New J. Phys.*, vol. 14, Mar. 2012, Art. no. 118001.

Jean Cavillot (Member, IEEE) was born in Arlon, Belgium, in 1994. He received the master's degree in electrical engineering and the Ph.D. degree from the Université Catholique de Louvain (UCLouvain), Ottignies-Louvain-la-Neuve, Belgium, in 2017 and 2021, respectively.

In 2017, he was working on the design of passive microwave mixers for radar applications at UCLouvain. He started his Ph.D. thesis under the Fonds pour la Formation à la Recherche dans l'Industrie et dans l'Agriculture (FRIA) Grant from the Fonds National de la Recherche Scientifique (FNRS) in 2018. He is currently a Post-Doctoral Researcher with UCLouvain, where he continues his research in the areas of finite antenna arrays and metasurfaces.

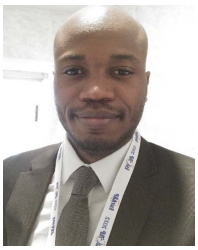

Modeste Bodehou (Member, IEEE) was born in Cotonou, Benin, in 1992. He received the B.Sc. degree in engineering and the M.Sc. degree in electrical engineering (telecommunications) from the Royal Military Academy, Brussels, Belgium, in 2013 and 2015, respectively, and the Ph.D. degree in engineering and technology, and the master's degree in management from the Université Catholique de Louvain, Ottignies-Louvain-la-Neuve, Belgium, in 2020 and 2022, respectively.

In 2015, he was with the Quartier Major Housiau (Belgium Defense), Vilvoorde, Belgium, where he was involved in the framework of his application school on military communication systems. He is currently a Fonds National de la Recherche Scientifique (FNRS) Post-Doctoral Researcher with the Microwave and Applied Electromagnetism Laboratory, Université Catholique de Louvain. His current research interests include computational electromagnetics, antenna arrays, and metasurfaces.

Dr. Bodehou was a recipient of the 2021 European Association on Antennas and Propagation (EurAAP) Per-Simon Kildal Award for the Best Ph.D. in Antennas and Propagation; the Best Student Paper Award at the 13th European Conference on Antennas and Propagation, Krakow, Poland, in 2019; the First Prize Student Paper Competition Award at the IEEE-Microwave Theory and Technology (MTT) International Conference on Numerical Electromagnetic and Multiphysics Modeling and Optimization for RF, Microwave, and Terahertz Applications, Seville, Spain, in 2017; and the Association Royale des Ingénieurs issus de l'Ecole d'Application de l'Artillerie et du Génie (AIA) Price for the Best Engineering Master Thesis Award from the Royal Military Academy, Brussels, Belgium, in 2015.

Christophe Craeye (Senior Member, IEEE) was born in Belgium, in 1971. He received the master's degree in electrical engineering and the B.Phil. degree from the Université Catholique de Louvain (UCLouvain), Ottignies-Louvain-la-Neuve, Belgium, in 1994, and the Ph.D. degree in applied sciences from UCLouvain in 1998.

From 1994 to 1999, he was a Teaching Assistant with UCLouvain and carried out research on the radar signature of the sea surface perturbed by rain, in collaboration with the National Aeronautics and Space Administration (NASA) and European Space Agency (ESA). From 1999 to 2001, he was a Post-Doctoral Researcher with the Eindhoven University of Technology, Eindhoven, The Netherlands. He was with the University of Massachusetts, Amherst, MA, USA, in 1999. He was with the Netherlands Institute for Research in Astronomy, Dwingeloo, The Netherlands, in 2001. In 2002, he started an antenna research activity with UCLouvain, where he is currently a Professor. He was with the Astrophysics and Detectors Group, University of Cambridge, Cambridge, U.K., in 2011. His research was funded by the Region Wallonne, the European Commission, ESA, the Fonds National de la Recherche Scientifique (FNRS), and UCLouvain. His current research interests include mutual coupling, finite antenna arrays, wideband antennas, small antennas, metamaterials, fast physical optics, and numerical methods for fields in periodic media, with applications to communication and sensing systems.

Dr. Craeye received the 2005–2008 Georges Vanderlinden Prize from the Belgian Royal Academy of Sciences in 2009. He was an Associate Editor of the IEEE TRANSACTIONS ON ANTENNAS AND PROPAGATION from 2004 to 2010 and the IEEE ANTENNAS AND WIRELESS PROPAGATION LETTERS from 2011 to 2017.